

# Synthetic gauge fields for phonon transport in a nano-optomechanical system

John P. Mathew<sup>1,2</sup>, Javier del Pino<sup>1,2</sup> and Ewold Verhagen<sup>1\*</sup>

**Gauge fields in condensed matter physics give rise to nonreciprocal and topological transport phenomena and exotic electronic states<sup>1</sup>. Nanomechanical systems are applied as sensors and in signal processing, and feature strong nonlinearities. Gauge potentials acting on such systems could induce quantum Hall physics for phonons at the nanoscale. Here, we demonstrate a magnetic gauge field for nanomechanical vibrations in a scalable, on-chip optomechanical system. We induce the gauge field through multi-mode optomechanical interactions, which have been proposed as a resource for the necessary breaking of time-reversal symmetry<sup>2–4</sup>. In a dynamically modulated nanophotonic system, we observe how radiation pressure forces mediate phonon transport between resonators of different frequencies. The resulting controllable interaction, which is characterized by a high rate and nonreciprocal phase, mimics the Aharonov–Bohm effect<sup>5</sup>. We show that the introduced scheme does not require high-quality cavities, such that it allows exploring topological acoustic phases in many-mode systems resilient to realistic disorder.**

Broken spatio-temporal symmetries can induce one-way transport and topological protection in bosonic systems<sup>6–8</sup>. Temporal modulation plays a role in those efforts, imparting direction-dependent phases on electrons<sup>9</sup> as well as chargeless excitations of cold atoms and ions<sup>10,11</sup>, light<sup>12,13</sup> and mechanics<sup>14,15</sup>. Breaking time-reversal symmetry, these phases mimic the action of magnetic gauge potentials on electrons, thus leading to the Aharonov–Bohm effect and the integer quantum Hall effect, which offers topologically protected transport in extended systems. This contrasts with mechanisms in structured passive linear media (for example, spin–orbit coupling), which enable on-chip topological mechanical states<sup>16</sup> but do not offer the level of protection associated with time-reversal symmetry breaking. Cavity optomechanics provides a natural platform to realize time-varying potentials for either photons or phonons and has recently been used to demonstrate nonreciprocal control<sup>3,4,17–21</sup>. In many-mode optomechanical lattices, similar principles would allow inducing topological phases of light and sound at the nanoscale<sup>2,22</sup>. However, these proposals require high quality factors and put extreme demands on fabrication tolerances and control intensities to achieve sufficiently strong interactions.

The mechanism we introduce overcomes these challenges to establish a magnetic gauge potential for sound at the nanoscale. It relies on optically mediated mode transfer and arises naturally in a system that dispersively couples two mechanical modes to a single optical cavity driven with a detuned laser<sup>23</sup>. One mechanical mode's displacement then shifts the cavity resonance, modifying the intra-cavity photon number and hence the radiation pressure on the second mode. This principle allows coherent mechanical transfer and entanglement<sup>24,25</sup>. Our experimental system consists of

a sliced photonic crystal nanobeam<sup>26</sup>, supporting a subwavelength optical defect mode of frequency  $\omega_c = 2\pi \times 192.36$  THz and linewidth  $\kappa = 2\pi \times 256$  GHz, coupled to the two  $\sim 2.4$  MHz frequency in-plane flexural modes of the beam halves (Fig. 1a,b).

To induce a gauge field, we introduce a frequency difference between the mechanical modes. Keeping the lengths of the beam halves dissimilar separates their frequencies  $\Omega_1$  and  $\Omega_2$  by  $\sim 0.5$  MHz—many times the mechanical linewidths  $\Gamma_i \simeq 2\pi \times 3$  kHz. Despite their disparate frequencies, the two mechanical modes can be coupled through time-varying forces<sup>21,24,25,27,28</sup>. By modulating the intensity of a drive laser incident from free space, the intra-cavity photon number evolves as  $n(t) = \bar{n}_c(1 + c_m \cos(\omega_m t + \phi_m) + \dots)$  with average population  $\bar{n}_c$ , frequency  $\omega_m$ , phase  $\phi_m$ , modulation depth  $c_m$  and dots denoting modulation overtones at  $(2k + 1)\omega_m$ ,  $k \in \mathbb{N}$ . The instantaneous response of the photon number—and thus radiation pressure—to the modulated laser is guaranteed by the large cavity linewidth, meaning operation in the bad-cavity limit  $\kappa \gg \Omega_{1,2}$ . After linearization around the photonic steady state and adiabatic elimination of the cavity dynamics, the coherent evolution of the phononic modes (annihilation operators  $\hat{b}_i$ ) within the resonance condition  $\omega_m = |\tilde{\Omega}_2 - \tilde{\Omega}_1|$  is governed by the effective Hamiltonian in the mechanical rotating frame ( $\tilde{b}_i = e^{i\tilde{\Omega}_i t} \hat{b}_i$ ):

$$\tilde{H}_{\text{eff}} = \hbar g_{\text{eff}} (\tilde{b}_1^\dagger \tilde{b}_2 e^{-i\phi_m} + \tilde{b}_2^\dagger \tilde{b}_1 e^{i\phi_m}) \quad (1)$$

For this derivation (Supplementary Section II) we assumed that higher-order mechanical modes and relevant modulation frequencies are incommensurable<sup>26</sup>.

In view of equation (1), the modulated cavity field provides an effective pathway to swap phonons between mechanical modes  $\hat{b}_1$  and  $\hat{b}_2$ , characterized by a nonreciprocal imprint of the modulation phase  $\phi_m$  for up/down mode conversion paths (Fig. 1c). As noted in photonics<sup>12,13,29,30</sup> and cold atoms<sup>10</sup>, the modulation phase plays the role of a Peierls phase<sup>6</sup> for a charged particle in a magnetic field, with an effective gauge potential,  $\mathbf{A}_{\text{eff}}$ , defined through  $\phi_m = \int_1^2 \mathbf{A}_{\text{eff}} d\mathbf{l}$ , where  $\mathbf{l}$  parametrizes the integration path. Although this naturally exhibits gauge freedom (that is, under local  $U(1)$  group operations  $\tilde{b}_i \rightarrow \tilde{b}'_i = e^{i\alpha_i} \tilde{b}_i$ ), the introduction of frequency conversion with controllable Peierls phases implements a finite gauge-invariant flux related to the phase accumulated over a closed (Aharonov–Bohm) loop. This flux can be tuned by varying a single-bond modulation phase, revealing the action of a gauge potential on the bond. Optical carrier phases play no role in this pseudo-magnetic field and leave the optically induced coupling rate  $g_{\text{eff}}$  unchanged.

Crucially, to leverage this gauge field,  $g_{\text{eff}}$  overcomes mechanical dissipation and frequency disorder. This is given by  $g_{\text{eff}} = c_m g_1 g_2 \Delta / (\Delta^2 + \kappa^2/4)$ , where  $\Delta = \omega_L - \omega_c$  is the laser detuning and  $g_i = g_{0i} \sqrt{\bar{n}_c}$  denotes the cavity-enhanced optomechanical

<sup>1</sup>Center for Nanophotonics, AMOLF, Amsterdam, The Netherlands. <sup>2</sup>These authors contributed equally: John P. Mathew, Javier del Pino.

\*e-mail: [verhagen@amolf.nl](mailto:verhagen@amolf.nl)

couplings for photon–phonon coupling rates  $g_{0i}$ . The cross-mode coupling  $g_{\text{eff}}$  has a similar origin to the optical spring effect, which shifts the mechanical frequencies to  $\tilde{\Omega}_i = \Omega_i + 2g_i^2\Delta/(\Delta^2 + \kappa^2/4)$  (see the discussion of transferred phase measurements in the following and Extended Data Fig. 1a–c for further details). It overcomes mechanical damping for detunings  $\Delta \simeq \pm\kappa/2$  if the cooperativity  $4g_i^2/(\kappa\Gamma_i)$  exceeds unity. This can be reached in the sliced nanobeam platform even for  $\bar{n}_c < 1$  and a large optical bandwidth<sup>26</sup>. In fact, our defining advantage is the ability to operate in the bad-cavity limit  $\kappa \gg \Omega_i$ —in contrast to other proposed mechanisms<sup>2,22</sup>—greatly relaxing the practical requirements for many-mode extensions as shown below.

In our experiment we measure mechanical motion by analysing intensity variations imprinted on a second ‘detection’ laser far detuned from the cavity, using cross-polarized direct reflection (Fig. 1d)<sup>26</sup>. The thermal fluctuation spectra of both modes are presented in Fig. 2a, showing optical spring shifts as the drive laser is tuned across cavity resonance. Subsequently, for a fixed detuning  $\hat{H}_d = \hbar\alpha_d\hat{b}_d e^{i\omega_d t} + \text{h.c.}$ , the driving intensity is modulated using the outputs of a lock-in amplifier to include a weak probe tone at frequency  $\omega_d$ , besides the control modulation (depth  $c_d \ll c_m$ ). Assuming, without loss of generality, that  $\tilde{\Omega}_2 \gg \tilde{\Omega}_1$ , mode 1 is driven if  $\omega_d \simeq \tilde{\Omega}_1$ . The strong tone at  $\omega_m \approx \Delta\tilde{\Omega} \equiv \tilde{\Omega}_2 - \tilde{\Omega}_1$  parametrically couples the two modes. Driven and transferred coherent responses of the mechanical modes are analysed by a lock-in measurement of the reflected detection laser intensity at frequencies  $\omega_d$  and  $\omega_t = \omega_d + \omega_m$ , respectively (see Methods). The outcome is captured by the driven/transferred linear susceptibilities in  $\langle \hat{b}_d(\omega_d) \rangle = \alpha_d \chi_d^{\uparrow\downarrow}(\omega_d)$  and  $\langle \hat{b}_i(\omega_t) \rangle = \alpha_i \chi_i^{\uparrow\downarrow}(\omega_t)$ , in response to a driving (optical amplitude  $\alpha_d \propto c_d$ )

$$\chi_1^{\uparrow}(\omega_d) = \frac{1 + g_{\text{eff}}\chi_2^{\uparrow}(\omega_d + \omega_m)}{\omega_d - (\tilde{\Omega}_1 - i\frac{\Gamma_1}{2})} \quad (2a)$$

$$\chi_2^{\uparrow}(\omega_d + \omega_m) = \frac{g_{\text{eff}}e^{i\phi_m}}{(\omega_d - z_+^{\uparrow})(\omega_d - z_-^{\uparrow})} \quad (2b)$$

where  $\uparrow, \downarrow$  label up and down transfer pathways and  $z_{\pm}^{\uparrow}$  are the roots of the characteristic polynomial of  $z^{\uparrow}$ :

$$\left[ z^{\uparrow} - \left( \tilde{\Omega}_1 - i\frac{\Gamma_1}{2} \right) \right] \left[ z^{\uparrow} - \left( \tilde{\Omega}_2 - \omega_m - i\frac{\Gamma_2}{2} \right) \right] - g_{\text{eff}}^2 \quad (3)$$

Without modulation ( $c_m = 0$ ), the coherent amplitude response of mode 1 is a single peaked function (Fig. 2b) and no transfer occurs. In contrast, for  $c_m g t \neq 0$ , the modulation frequency approaching resonance ( $\omega_m = \Delta\tilde{\Omega}$ ) reveals strong coupling with splitting of the mechanical response of mode 1 and non-zero transfer to mode 2. At the highest modulation strength ( $c_m = 0.98$ ), strong coupling with mode hybridization is observed and predicted (Fig. 2c). Here  $|\chi_1^{\uparrow}(\omega_d)|, |\chi_2^{\uparrow}(\omega_d + \omega_m)|$  display anticrossings with resonant Rabi splitting of  $\Omega_R^{\text{eff}} = \sqrt{4g_{\text{eff}}^2 - (\Gamma_1 - \Gamma_2)^2/4}$ . The strength of this dynamical strong coupling is tunable with optical power ( $g_{\text{eff}} \propto P_{\text{in}}$ ), and coupling rates as high as 4% of the mechanical frequencies are measured experimentally (Extended Data Fig. 2a,b). These large, tunable coupling rates, far exceeding achievable mechanical line-widths of  $\sim 2\pi \times 100\text{ Hz}$  (ref. 26), emphasize the potential of nanophotonic control to induce non-trivial forms of nanomechanical transport. We note that these phenomena rely on classical-waves coherence ( $\Omega_R^{\text{eff}} \gg \Gamma_m$ ). Their application to quantum acoustic signals requires overcoming thermal decoherence ( $\Omega_R^{\text{eff}} g t \bar{n}_{\text{th}} \Gamma_m$ , Bose occupation  $\bar{n}_{\text{th}}$ ), which is potentially reachable in mK environments.

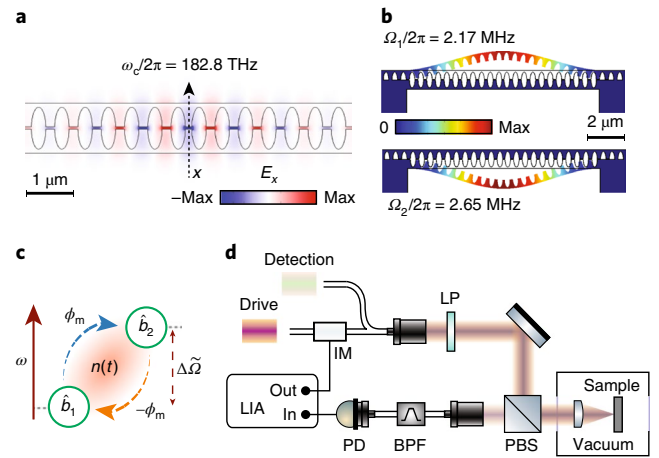


**Fig. 1 | Optomechanical system for synthetic nanomechanical gauge fields.** **a**, Simulated transverse electric field ( $E_x$ ) profile of the fundamental cavity mode of the sliced photonic crystal nanobeam employed in the experiment, tightly confined in the middle gap. **b**, Displacement profile (exaggerated) of the mechanical modes employed in the experiment. **c**, Time-modulated radiation pressure induces a synthetic gauge field for phonon transfer between modes of different frequency: the modulation phase is transferred nonreciprocally along opposite paths. Symbols are defined in the text. **d**, Schematic of the experimental set-up. IM, intensity modulator; LP, linear polarizer; PBS, polarizing beamsplitter; BPF, optical bandpass filter; PD, photodiode; LIA, lock-in amplifier. The LIA ports serve to (Out) drive the IM through an amplification stage (not shown) and to (In) analyse coherent intensity modulations of the detection laser.

To experimentally address the nanomechanical transfer phase and the tunability of the gauge potential, the phase of the lock-in signal at  $\omega_t$ , denoted  $\phi^{\uparrow\downarrow}$ , was measured as a function of  $\phi_m$  for a fixed set  $\omega_d, \omega_m, c_m$  to achieve resonant transfer (Fig. 3a). Because the input and detected phases evolve at different frequencies ( $\omega_d$  and  $\omega_d \pm \omega_m$ ), they cannot be unambiguously determined. They essentially depend on the (arbitrary) choice of time origin, reflecting the underlying gauge freedom. In contrast, the sum over phases around the loop that includes the measurement apparatus is a gauge-invariant quantity mimicking a magnetic flux piercing the loop. This can be tuned by varying  $\phi_m$  if the latter indeed takes the role of a Peierls phase. The very same fingerprint of time-reversal symmetry breaking is revealed by the phase difference between two paths forming the loop, measured with two opposite orientations. These paths include, respectively, (1) the nanomechanical transport path with controlled gauge potential (plus the optical/electronic input and output signals) and (2) the electronic local oscillator (LO) with which the detected signal is compared in the lock-in amplifier (Supplementary Sections I and IV). Coherent mixing of both paths is possible as probe, modulation and LO signals are referenced to the same clock in the lock-in amplifier. The LO phase is calibrated such that the measured phase vanishes if  $\phi_m = 0$ . This allows control of the synthetic flux via the optomechanical link phase  $\phi_m$  while keeping the LO phase fixed (see Methods). Such an approach thus identifies a Peierls phase acting on the nanomechanical transport, via a sign flip for the reversed path orientation  $1 \leftrightarrow 2$ , and provides an univocal demonstration of a synthetic gauge field.

In Fig. 3a, the transfer phase is seen to accumulate nonreciprocally during up- and downconversion, in agreement with equation (1), proving that time-modulated radiation pressure induces a magnetic field for phononic transport. To further investigate the impact of the cavity mode, we measured the out-of-phase quadrature (see Methods) of the transferred response as a function of optical frequency for both conversion pathways,  $Y_t^{\uparrow\downarrow}$ .

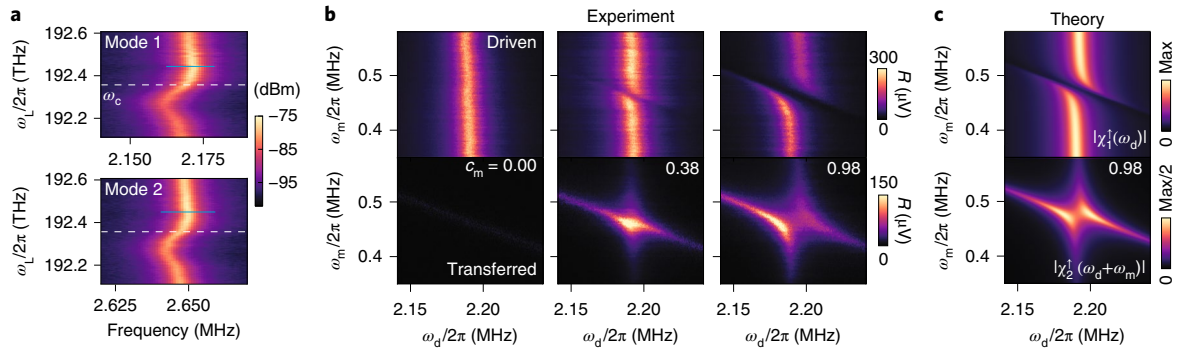


**Fig. 2 | Optically mediated phonon conversion.** **a**, Thermomechanical noise spectra of the two mechanical modes imprinted on the detection laser as the (unmodulated) drive laser frequency is swept across the cavity resonance. The mechanical modes are seen to be tuned via the optical spring shift. The white dashed lines denote the cavity frequency  $\omega_c$ , and the blue lines denote the drive laser frequency used in subsequent measurements. The input power of the drive laser was locked to  $P_{in} = 33.4 \mu\text{W}$  (see Methods). **b**, Amplitude of the driven response of mode 1 and simultaneously measured transferred response to mode 2 as a function of the modulation frequency for different modulation strengths  $c_m$ . The lock-in measurement of the detection laser intensity modulation at  $\omega_d \simeq \tilde{\Omega}_1$  gives the driven response, while demodulation at  $\omega_d + \omega_m \simeq \tilde{\Omega}_2$  gives the transferred response. For  $c_m = 0$ , there is no coherent transfer and only a faint thermal noise of mode 2 is observed. Transfer to mode 2 occurs in the vicinity of  $\omega_m \approx \Delta\tilde{\Omega}$ . At large modulation strengths, a clear splitting is observed in the response. **c**, Theoretical response plots of the absolute value of the susceptibility function for each mode for  $c_m = 0.98$  with phenomenological linewidths  $\Gamma_i/2\pi = \{8.1, 8.6\}$  kHz (see Methods), where  $\text{max} = \text{max}(|\chi_i^\dagger|)$ . The incident power in **b** and **c** is  $P_{in} = 174 \mu\text{W}$ .

In fact, a calculation reveals that this quantity is gauge-invariant and sensitive to the nonreciprocity of the transferred phase, namely  $Y_t^{\uparrow\downarrow}(\omega_L, \phi_m) \propto \text{Im}\chi_t^{\uparrow\downarrow} = |\chi_t^{\uparrow\downarrow}| \sin(\pm\phi_m + \varphi^{\uparrow\downarrow}(\omega_L))$ , where

$$\varphi^{\uparrow\downarrow}(\omega_L) = \arg[\chi_t^{\uparrow\downarrow}] \Big|_{\phi_m=0} \quad (\text{Supplementary Section IV}).$$

In Fig. 3b, phase nonreciprocity ( $\phi^\uparrow = \phi_m = -\phi^\downarrow$ ) flips the sign in the optical quadrature for resonant up/down transfer processes ( $\omega_m = \Delta\tilde{\Omega}$ ), owing to  $\text{Im}\chi_2^\dagger(\omega_d^\uparrow + \omega_m) = -\text{Im}\chi_1^\dagger(\omega_d^\downarrow - \omega_m) = g_{\text{eff}} \sin \phi_m / (g_{\text{eff}}^2 + \Gamma_1\Gamma_2/4)$ ,

where  $\omega_d^{\uparrow\downarrow} = \tilde{\Omega}_{1,2}$ . A similar phenomenon holds for transient signals transferred between two modes (for further details see Supplementary Section V). Optimal transfer amplitude occurs when the optical spring effect is maximal, with a sizable bandwidth determined by the spring shift of mechanical modes out of resonance for fixed  $\omega_d, \omega_m$ , yielding non-zero accumulated phases  $\varphi^{\uparrow\downarrow}$  and the breakdown of ideal nonreciprocity ( $\phi^\uparrow \neq -\phi^\downarrow$ ).

By virtue of the bad-cavity limit operation of our optomechanical mechanism, the tolerances for nanobeam fabrication (see below) and the ability to optically control transport via out-of-plane illumination, the two-mode set-up has high potential to be scaled up by suitably assembling many nanobeams. A synthetic gauge field for phonon transport could then enable artificial engineering of topological phases in extended systems that connect nanobeam resonators through THz-linewidth optical modes. As an example, we consider the two-dimensional (2D) network of nanobeams depicted in Fig. 4a. Each mechanical mode links to three nearest neighbours of the other flavour (frequency) via modulated cavities, assembling a honeycomb lattice with tunable links. A spatially varying phase pattern in the hopping terms (for example using spatial light modulators) mimicks a magnetic flux piercing the lattice. In particular, the choice  $\phi_{ij} = 2\pi\mathbf{r}_{ij} \cdot \mathbf{a}_2 p / (aq)$  along a unit vector  $\mathbf{a}_2$ , where  $a$  is the lattice normalization constant and  $p$  and  $q$  are coprime integers (Fig. 4b) emulates the Landau gauge for an off-plane constant magnetic flux  $\Phi_{\text{eff}} = 2\pi p/q$ , permeating each plaquette. The 2D extension of the resonant Hamiltonian in equation (1) leads to the Harper–Hofstadter model<sup>6</sup>:

$$\tilde{H}_{\text{eff}}^{\text{lat}} = \hbar g_{\text{eff}} \sum_{(i,j) \in \text{n.n.}} \tilde{b}_1^{(i)\dagger} \tilde{b}_2^{(j)} e^{-i\phi_{ij}} + \text{h.c.} \quad (4)$$

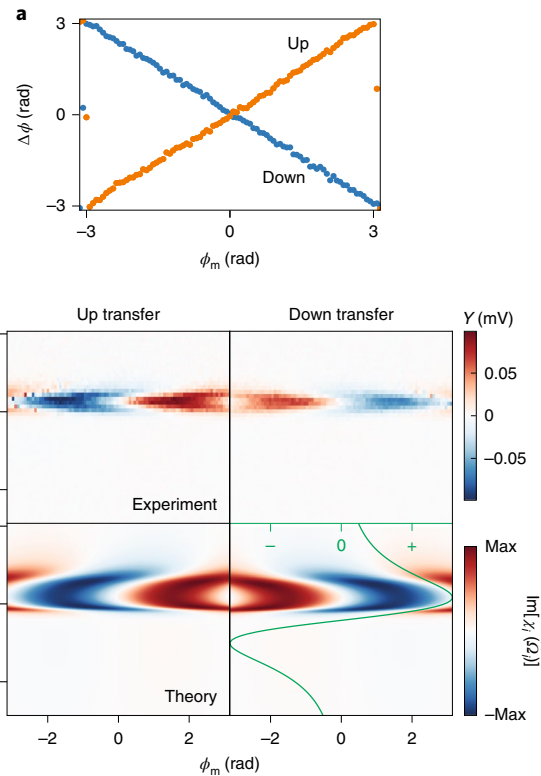


**Fig. 3 | Nonreciprocal phase imprint.** **a**, Phase measured at the frequency of the transferred mode for the up and down transfer processes as a function of the modulation phase,  $\phi_m$ , referenced to the transfer phase at  $\phi_m = 0$ . The optically induced gauge field imprints a nonreciprocal modulation phase on the transfer. **b**, The out-of-phase response of the two conversion paths as a function of the modulation phase and drive laser detuning. The calculated response shows the imaginary part of the susceptibility of the transferred mode. The green curve and corresponding axis denote the calculated optical spring shift. For these measurements, the phase calibration procedure is followed at  $\omega_L/2\pi = 192.45$  THz (see Methods). The modulation strength is  $c_m = 0.38$  in **a** and **b**.

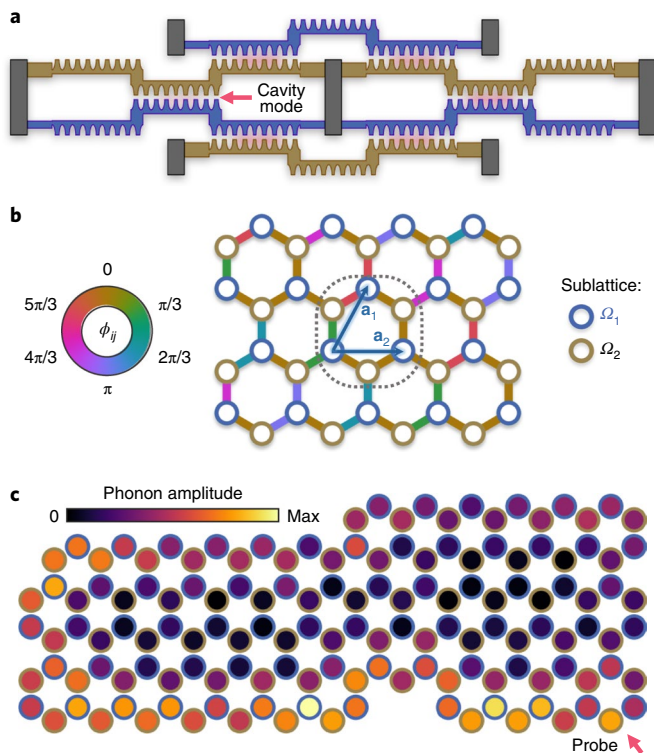


**Fig. 4 | Extended optomechanical nanobeam lattice.** **a**, Proposed experimental implementation of a topological nanobeam array. Nanobeams of different frequency are colour-coded, with grey rectangles depicting supports. Each nanobeam is interconnected to three nanobeams of different frequency via broadband nanophotonic cavities. **b**, This structure forms a honeycomb plaquette (surrounded by a dashed line), where each circle denotes an entire arm. By repetition, a honeycomb lattice with primitive lattice vectors  $\mathbf{a}_1$ ,  $\mathbf{a}_2$  is formed. The optical modulation phases to create a specific topological insulator phase, defined in the text, are indicated by the colours of the links. **c**, Simulated steady-state phononic amplitude under continuous driving, focused on the site indicated by an arrow. Chosen parameters are  $\Gamma_1/2\pi = \Gamma_2/2\pi = 4.5$  kHz,  $g_{\text{eff}}/2\pi = 200$  kHz, phononic frequency disorder with standard deviation  $\sigma_\Omega/2\pi = 20$  kHz and direct mechanical coupling of  $t_2/2\pi = 10$  kHz.

Non-trivial topological properties are then observed for rational  $p/q$  ( $= 1/3$  in the following), where the bandstructure for an infinite ribbon geometry shows  $2q$  bulk bands split into  $2q - 2$  gaps, traversed by (chiral) counter-propagating edge modes (see top panel in Extended Data Fig. 2c). To exemplify phononic propagation along the boundary of a finite array, we calculate the steady state while driving an edge site (see Methods). A moderate frequency disorder of  $\sim 1\%$  is introduced, in addition to direct mechanical coupling of  $\sim t_2 \sum_{(i,j) \in \text{n.n.n.}} \sum_{l=1,2} (\tilde{b}_l^{(i)\dagger} \tilde{b}_l^{(j)} + \text{h.c.})$  linking next-nearest neighbours<sup>26</sup>. As shown by the calculated amplitudes in Fig. 4c, emerging phononic edge modes display unidirectional propagation within state-of-the-art fabrication tolerances (see Supplementary Section III and Extended Data Fig. 2c–e for more details). This demonstrates a feasible platform for nanoscale phononic topological insulators based on optically induced magnetic fields.

In conclusion, we have established a synthetic gauge field for nanomechanical transport using optically mediated couplings in an optomechanical system. We have introduced an experimental platform with large optomechanical interactions and bandwidths that unlocks many-mode implementations in the nanomechanical domain. The tunability of our system allows the investigation of

physics beyond the rotating wave approximation and in synthetic dimensions<sup>31</sup>. Out-of-plane optical control provides a counterpart to electromechanical methods<sup>32,33</sup> with unique traits. It offers prospects for exploring the impact of thermal and quantum fluctuations on topologically protected phonon transport<sup>21</sup> and the effects of mechanical or optomechanical nonlinearities<sup>26</sup>. It is an advance towards exploiting topologically protected sound in the quantum acoustics regime and the search for exotic states such as those produced by non-Abelian gauge fields and analogues of the fractional quantum Hall effect<sup>30</sup> in the realm of nanomechanics.

### Online content

Any methods, additional references, Nature Research reporting summaries, source data, extended data, supplementary information, acknowledgements, peer review information; details of author contributions and competing interests; and statements of data and code availability are available at <https://doi.org/10.1038/s41565-019-0630-8>.

Received: 16 January 2019; Accepted: 18 December 2019;  
Published online: 03 February 2020

### References

- Laughlin, R. B. Quantized Hall conductivity in two dimensions. *Phys. Rev. B* **23**, 5632 (1981).
- Peano, V., Brendel, C., Schmidt, M. & Marquardt, F. Topological phases of sound and light. *Phys. Rev. X* **5**, 031011 (2015).
- Ruesink, F., Miri, M.-A., Alù, A. & Verhagen, E. Nonreciprocity and magnetic-free isolation based on optomechanical interactions. *Nat. Commun.* **7**, 13662 (2016).
- Fang, K. et al. Generalized non-reciprocity in an optomechanical circuit via synthetic magnetism and reservoir engineering. *Nat. Phys.* **13**, 465–471 (2017).
- Aharonov, Y. & Bohm, D. Significance of electromagnetic potentials in the quantum theory. *Phys. Rev.* **115**, 485–491 (1959).
- Ozawa, T. et al. Topological photonics. *Rev. Mod. Phys.* **91**, 015006 (2019).
- Goldman, N., Budich, J. & Zoller, P. Topological quantum matter with ultracold gases in optical lattices. *Nat. Phys.* **12**, 639–645 (2016).
- Huber, S. D. Topological mechanics. *Nat. Phys.* **12**, 621–623 (2016).
- Lindner, N. H., Refael, G. & Galitski, V. Floquet topological insulator in semiconductor quantum wells. *Nat. Phys.* **7**, 490–495 (2011).
- Dalibard, J., Gerbier, F., Juzeliūnas, G. & Öhberg, P. Colloquium: Artificial gauge potentials for neutral atoms. *Rev. Mod. Phys.* **83**, 1523–1543 (2011).
- Bermudez, A., Schaetz, T. & Porras, D. Synthetic gauge fields for vibrational excitations of trapped ions. *Phys. Rev. Lett.* **107**, 150501 (2011).
- Fang, K., Yu, Z. & Fan, S. Photonic Aharonov–Bohm effect based on dynamic modulation. *Phys. Rev. Lett.* **108**, 153901 (2012).
- Fang, K., Yu, Z. & Fan, S. Realizing effective magnetic field for photons by controlling the phase of dynamic modulation. *Nat. Photon.* **6**, 782–787 (2012).
- Nash, L. M. et al. Topological mechanics of gyroscopic metamaterials. *Proc. Natl Acad. Sci. USA* **112**, 14495–14500 (2015).
- Wang, Y. et al. Observation of nonreciprocal wave propagation in a dynamic phononic lattice. *Phys. Rev. Lett.* **121**, 194301 (2018).
- Cha, J., Kim, K. W. & Daraio, C. Experimental realization of on-chip topological nanoelectromechanical metamaterials. *Nature* **564**, 229–233 (2018).
- Shen, Z. et al. Experimental realization of optomechanically induced non-reciprocity. *Nat. Photon.* **10**, 657–661 (2016).
- Peterson, G. A. et al. Demonstration of efficient nonreciprocity in a microwave optomechanical circuit. *Phys. Rev. X* **7**, 031001 (2017).
- Bernier, N. R. et al. Nonreciprocal reconfigurable microwave optomechanical circuit. *Nat. Commun.* **8**, 604 (2017).
- Xu, H., Mason, D., Jiang, L. & Harris, J. Topological energy transfer in an optomechanical system with exceptional points. *Nature* **537**, 80–83 (2016).
- Xu, H., Jiang, L., Clerk, A. A. & Harris, J. G. E. Nonreciprocal control and cooling of phonon modes in an optomechanical system. *Nature* **568**, 65–69 (2019).
- Walter, S. & Marquardt, F. Classical dynamical gauge fields in optomechanics. *New J. Phys.* **18**, 113029 (2016).
- Shkarin, A. et al. Optically mediated hybridization between two mechanical modes. *Phys. Rev. Lett.* **112**, 013602 (2014).
- Weaver, M. J. et al. Coherent optomechanical state transfer between disparate mechanical resonators. *Nat. Commun.* **8**, 824 (2017).

25. Ockeloen-Korppi, C. et al. Stabilized entanglement of massive mechanical oscillators. *Nature* **556**, 478–482 (2018).
  26. Leijssen, R., La Gala, G. R., Freisem, L., Muhonen, J. T. & Verhagen, E. Nonlinear cavity optomechanics with nanomechanical thermal fluctuations. *Nat. Commun.* **8**, 16024 (2017).
  27. Okamoto, H. et al. Coherent phonon manipulation in coupled mechanical resonators. *Nat. Phys.* **9**, 480–484 (2013).
  28. Faust, T., Rieger, J., Seitner, M. J., Kotthaus, J. P. & Weig, E. M. Coherent control of a classical nanomechanical two-level system. *Nat. Phys.* **9**, 485–488 (2013).
  29. Tzuang, L. D., Fang, K., Nussenzeig, P., Fan, S. & Lipson, M. Non-reciprocal phase shift induced by an effective magnetic flux for light. *Nat. Photon.* **8**, 701–705 (2014).
  30. Roushan, P. et al. Chiral ground-state currents of interacting photons in a synthetic magnetic field. *Nat. Phys.* **13**, 146–151 (2017).
  31. Celi, A. et al. Synthetic gauge fields in synthetic dimensions. *Phys. Rev. Lett.* **112**, 043001 (2014).
  32. Hatanaka, D., Mahboob, I., Onomitsu, K. & Yamaguchi, H. Phonon waveguides for electromechanical circuits. *Nat. Nanotechnol.* **9**, 520–524 (2014).
  33. Cha, J. & Daraio, C. Electrical tuning of elastic wave propagation in nanomechanical lattices at MHz frequencies. *Nat. Nanotechnol.* **13**, 1016–1020 (2018).
- Publisher's note** Springer Nature remains neutral with regard to jurisdictional claims in published maps and institutional affiliations.
- © The Author(s), under exclusive licence to Springer Nature Limited 2020

## Methods

**Fabrication.** The devices were fabricated from a silicon-on-insulator substrate, with a 250 nm device layer and 3  $\mu\text{m}$  buried oxide layer (BOX). A 75 nm layer of diluted hydrogen silsesquioxane resist (1:2 in methyl isobutyl ketone) was spin-coated, and electron-beam lithography was used to write patterns on the sample. After developing in tetramethylammonium hydroxide, an anisotropic etch of the exposed device layer was performed using inductively coupled plasma-reactive ion etching in the presence of HBr and  $\text{O}_2$  gases. Finally, suspended nanobeams were obtained after a wet etch of the underlying BOX layer with hydrofluoric acid followed by critical point drying.

**Experimental set-up.** The sample was placed in a vacuum chamber at room temperature and pumped down to a pressure of  $\sim 2 \times 10^{-6}$  mbar. The devices were illuminated from outside the vacuum chamber using a broadband source and imaged in transmission on a phosphor-coated near-infrared camera (imaging components are omitted in Fig. 1d). A tunable laser (Toptica CTL 1500) connected through a Thorlabs LN81S-FC intensity modulator (IM) was used as the drive laser, and a second laser (New Focus TLB-6728) far detuned from the cavity resonance ( $\omega_L/2\pi = 191.68$  THz) was used as the detection laser. The lasers were combined on a fibre-based beam combiner and launched using a fibre collimator into the free-space set-up. Optical spring shifts were measured keeping the drive laser power locked by sampling the power in the free-space path and feedback control on the bias port of the IM (power stabilization is omitted in Fig. 1d). Power stabilization was turned off for mode transfer measurements in order to operate the modulator at the optimal point (Supplementary Section IV). The two outputs of the lock-in amplifier carrying signals at  $\omega_d$  and  $\omega_m$  were combined, amplified (Mini Circuits ZHL-32A+ with 10 dB attenuation) and connected to the RF port of the IM to drive and modulate the nanobeam mechanics. The IM response ( $V_\pi = 5.33$  V) and input amplification were characterized to quantify the modulation coefficients. The reflected detection laser was fibre-coupled, filtered using a tunable bandpass filter (DiCon), and detected on a fast, low-noise photodetector. Intensity modulations of the detection laser were analysed using a Zurich Instruments UHFLI lock-in amplifier.

**Phase calibration and testing nonreciprocity.** As we show below, measurement of the accumulated phase displayed in Fig. 3 involves a comparison of signals at the same frequency that are referenced to the same clock, allowing experimental determination of the transfer phase at a given choice of gauge. To explicitly show how this works, we tracked the signal path followed from excitation to detection. From the output ports of the lock-in amplifier, the modulation and probe voltage tones  $V_m = \cos(\omega_m t + \phi_m + \theta_m)$  and  $V_d = \cos(\omega_d t + \phi_d + \theta_d)$  emerge at frequencies  $\{\omega_m, \omega_d\}$ , phases  $\{\phi_m, \phi_d\}$  as set in the lock-in amplifier, and 'random' initial phase offsets  $\{\theta_m, \theta_d\}$  (without loss of generality, we assume  $\omega_d \simeq \bar{\Omega}_1$  and  $\omega_d + \omega_m \simeq \bar{\Omega}_2$ ). Intensity modulations of the drive laser give rise to phonon transfer that excites the second mode. Optomechanically induced conversion can be effectively seen as mixing of the two tones, generating an electronic signal at frequency  $\bar{\Omega}_2$  from intensity modulations of the detection laser. Along this process, a phase that depends on the modulation tone via a general function  $\phi_t = \phi_t(\phi_m)$ , which is to be experimentally determined, is transferred coherently according to equation (1). The conversion signal is demodulated and the phase difference with respect to the set phase  $\phi_{LO}$  of a LO in the lock-in amplifier, which evolves as  $V_{LO} = \cos(\bar{\Omega}_2 t + \phi_{LO} + \theta_{LO})$ , is measured ( $\theta_{LO}$  is the random initial phase offset of the LO). The phase difference as measured by the demodulator is then given by  $\Delta\phi = \theta_d + \theta_m + \phi_t(\phi_m) - \phi_{LO} - \theta_{LO}$ , where  $\theta_p$  is the fixed propagation phase of the signal at frequency  $\bar{\Omega}_2$ , and propagation phases of the signals at  $\omega_m$  and  $\omega_d$  are absorbed in the random phases  $\theta_m$  and  $\theta_d$  without loss of generality.

For simplicity we set  $\phi_d = 0$  for all measurements and calibrate the LO phase to attain  $\Delta\phi = 0$  for the choice  $\phi_m = 0$ . This setting yields the calibration value  $\bar{\phi}_{LO} = \phi_d + \theta_d + \theta_m + \phi_t(0) - \theta_{LO}$ . Subsequently, for a non-zero  $\phi_m$ , the transferred phase shift is measured to be

$$\Delta\phi|_{\phi_{LO}=\bar{\phi}_{LO}} = \phi_t(\phi_m) - \phi_t(0) \quad (5)$$

independent of initial offsets and directly providing information about the transferred phase. During the measurements reported in Fig. 3, all above mentioned phases remain constant (to within a drift of  $\sim 3^\circ$  at maximum), except for  $\phi_t$  and  $\phi_m$ . This is guaranteed by the purity of the signal derived from the lock-in amplifier and checked independently. This configuration is crucial, as it allows us to govern and characterize the synthetic magnetic flux in the system by tuning  $\phi_m$  only (Supplementary Sections I and IV). The same procedure is

then followed for the down transfer measurement, providing a direct test of nonreciprocity by effectively changing the excitation–detection path orientation.

**Mechanical linewidth broadening.** For the driven measurements presented here, the mechanical linewidths are observed to be larger than the intrinsic damping rates of  $\sim 2\pi \times 3$  kHz. The subwavelength confinement of the optical mode and its co-localization with the mechanical modes causes sizable optomechanical cooperativities in our devices. In this scenario, the thermal motion of the mechanical modes causes large cavity frequency fluctuations of the order of  $\kappa$ , which in turn causes the optical spring shift to fluctuate. This leads to a broadening of the mechanical spectra beyond the intrinsic damping rate<sup>26</sup> and is captured in the model by using phenomenological linewidths  $\sim 2\pi \times 8$  kHz. This spectral broadening can be overcome by increasing the optical linewidths or cooling the devices to reduce the effect of fluctuations.

**Simulation details for edge state propagation.** In our model, localized intensity modulations of the cavity field at site  $\mathbf{r}_0$  of the phononic lattice induce an effective continuous wave-driving of the form  $\hat{H}_d = \boldsymbol{\alpha}_d(\omega_d, \mathbf{r}_0) \cdot \boldsymbol{\beta} e^{-i\omega_d t} + \text{h.c.}$ , such that  $\boldsymbol{\alpha}_d(\omega_d, \mathbf{r}_0) \approx \cos(\omega_d t) e^{-|\mathbf{r}_0|^2/w^2}$ , where  $w$  denotes the spot diameter and  $\omega_d$  is the frequency of the driving (exciting) modulation. Here,  $\boldsymbol{\beta}$  is a vector encompassing annihilation operators for localized mechanical modes at different sites. The steady-state phononic amplitude ( $\mathbf{u}_s$ ), in the presence of phononic frequency disorder and next-nearest-neighbour couplings, obeys the sparse linear system (writing  $\hat{H}_{\text{eff}}^{\text{lat}} = \boldsymbol{\beta}^\dagger \mathcal{A} \boldsymbol{\beta}$ )

$$\mathcal{A} \mathbf{u}_{\text{ss}} = \boldsymbol{\alpha}_d(\omega_d, \mathbf{r}_0) \quad (6)$$

where the calculation of the matrix  $\mathcal{A}$  is facilitated by use of the Kwant open-source package<sup>28</sup>. Disorder in photonic-mediated couplings is set to zero in this calculation, as it could be counterbalanced by intensity tuning of the incoming field (which could be derived from a single laser through judicious spatial structuring of the amplitude and phase of its modulation sideband).

## Data availability

The data that support the plots within this paper and other findings of this study are available from the open-access repository Zenodo, with assigned digital object identifier (DOI) 10.5281/zenodo.3554024.

## Code availability

The computer codes that support the plots within this paper and other findings of this study are available from the corresponding authors upon reasonable request.

## References

- Groth, C. W., Wimmer, M., Akhmerov, A. R. & Waintal, X. Kwant: a software package for quantum transport. *New J. Phys.* **16**, 063065 (2014).

## Acknowledgements

This work is part of the research programme of the Netherlands Organisation for Scientific Research (NWO). The authors acknowledge support from the Office of Naval Research (grant no. N00014-16-1-2466), the European Research Council (ERC starting grant no. 759644-TOPP) and the European Union's Horizon 2020 research and innovation programme under grant agreement no. 732894 (FET Proactive HOT).

## Author contributions

J.P.M. performed the experiments and analysed the data. J.d.P. developed the theoretical model. E.V. supervised the project. All authors contributed to the interpretation of results and writing of the manuscript.

## Competing interests

The authors declare no competing interests.

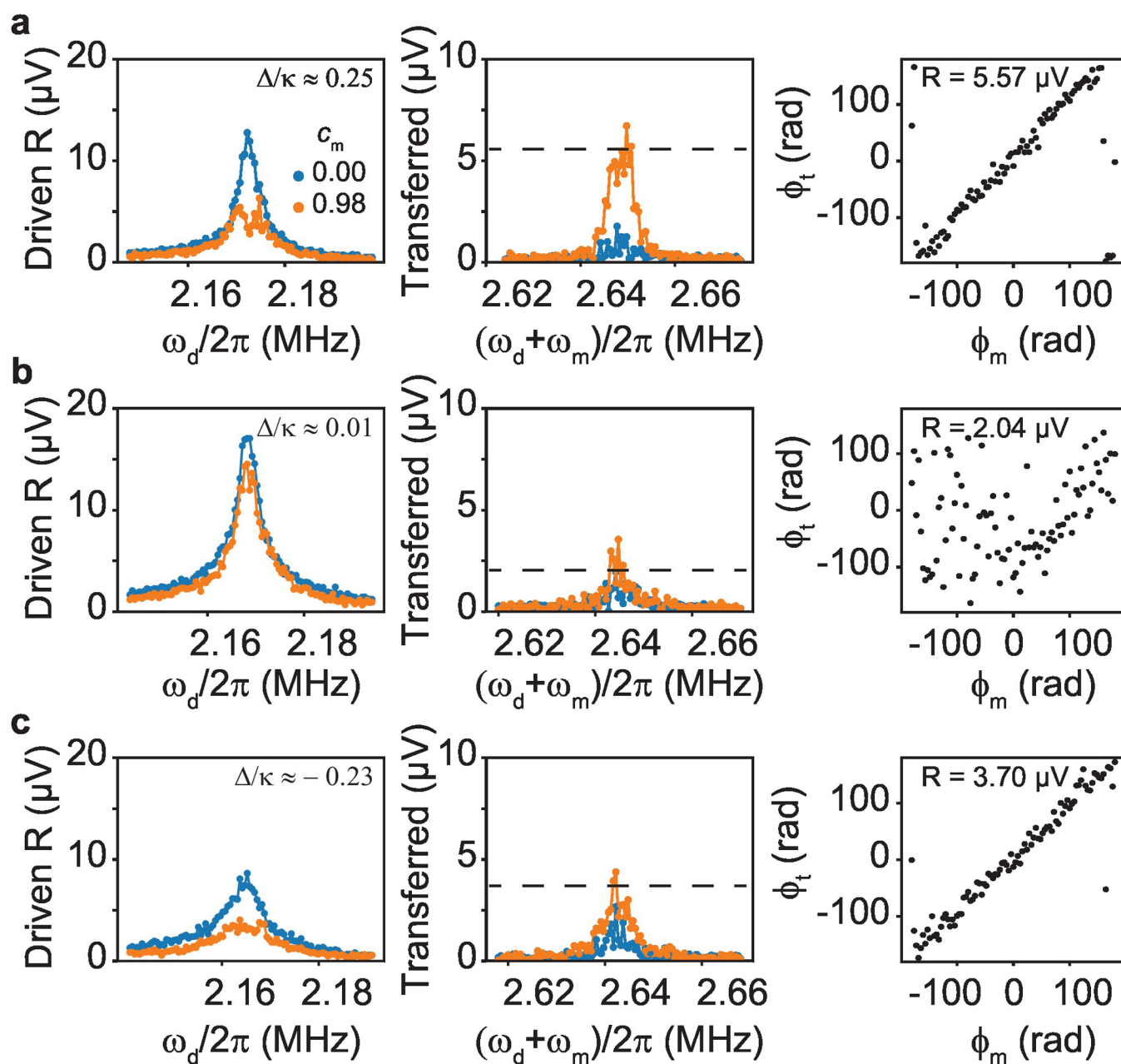
## Additional information

**Extended data** is available for this paper at <https://doi.org/10.1038/s41565-019-0630-8>.

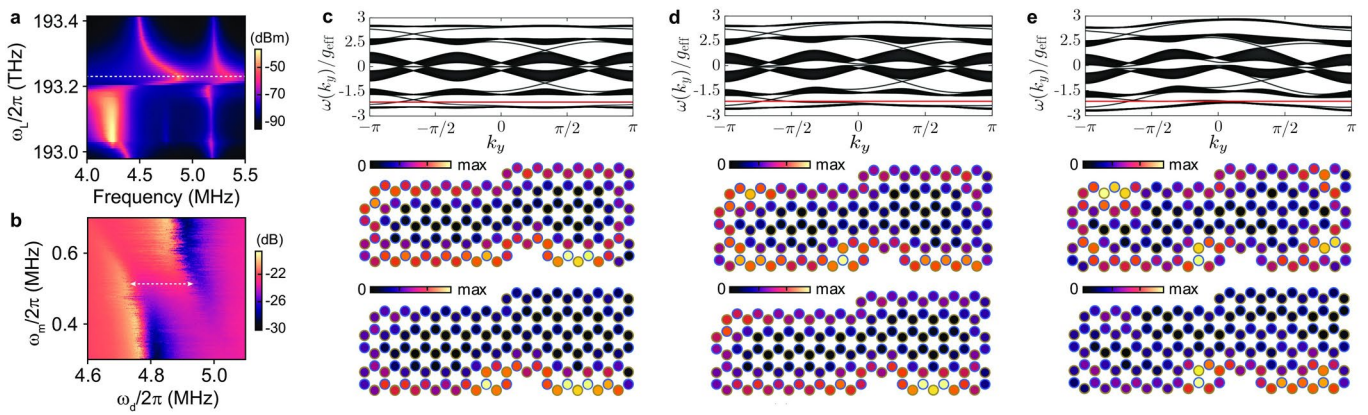
**Supplementary information** is available for this paper at <https://doi.org/10.1038/s41565-019-0630-8>.

**Correspondence and requests for materials** should be addressed to E.V.

**Reprints and permissions information** is available at [www.nature.com/reprints](http://www.nature.com/reprints).



**Extended Data Fig. 1 | Detuning dependent phonon transfer. a,b,c**, Mode transfer measurements for a detuning of  $\Delta/k \approx 0.25, 0.01,$  and  $-0.23$  respectively. The left two panels show the driven response of mode 1 and simultaneously measured transferred response to mode 2 for a fixed  $\omega_m$  chosen at each detuning. The phase imprint on mode 2 as a function of the modulation phase is shown in the rightmost panels. There is no clear phase pickup for near-zero detuning of the drive laser. The dashed line in the transferred response corresponds to the average magnitude of the transfer signal measured during the phase transfer measurement.



**Extended Data Fig. 2 | Robust phononic edge states.** **a**, Optical spring shift measured at higher optical powers for a separate device shows large tunability of the mechanical modes. The dashed, white line shows the drive laser detuning used in **b**. The unusual features between 193.0 and 193.2 THz are due to a dynamically unstable regime of potential photothermoelastic origin. **b**, The modulated coupling strength,  $g_{\text{eff}}$ , is higher for higher optical powers. The largest modulated coupling strength measured in our experiments is marked by the dashed line and seen to be  $\sim 2\pi \times 200$  kHz. Here the detection laser was absent and the drive laser response was directly demodulated using the lock-in amplifier leading to a Fano shaped feature for the driven response. **c,d,e**, (top panels) Band structure for a ribbon geometry (width  $L = 20$ ) for increasing values of the direct mechanical coupling from left to right (0, 10, and 20 kHz, respectively), displaying the driving modulation frequency. The steady-state phononic amplitude in the absence of disorder is displayed in the middle row, while the result with a phononic frequency disorder with standard deviation  $\sigma_\Omega/2\pi = 20$  kHz (averaged over 100 realizations) is shown at the bottom. For these plots,  $p/q = 1/3$ .